Supporting Online Material

Materials and Methods

Our iterative maximum a posteriori (IMAP) DOAS algorithm (*12*) is based on optimal estimation (*S1*,*S2*) and uses the depth of the absorption structures of the respective trace gases to deduce their abundances (see Fig. S4). Spectral parameters are taken from the HITRAN database (*S3*) with modifications for CH_4 line broadening parameters (*S4*) and CO_2 line strengths (*S5*). In brief, the algorithm iterates the slant column densities (SCD, concentration integrated along the light path) of all absorbers until their overall optical density best matches the measured optical density. Supposing that no clouds or aerosols in the atmosphere lead to enhanced scattering (*S6*), we can exactly derive the desired vertical column densities by dividing the retrieved SCD by the geometric air mass factor (AMF, the ratio of the length of the actual and the vertical light path). For our retrieval, we use a spectral window of 1630-1670 nm for CH_4 and 1562-1585 nm for CO_2. The precision errors in a single set of CH_4 and CO_2 VCD retrievals due to uncertainties in the fit are approximately 1.5% and 1%, respectively. Errors induced by clouds and aerosols in the field of view are far larger. However, rationing by CO_2 eliminates this source of error since the retrieved CO_2 VCD can be used as proxy for the light-path, analogous to O_2 in other applications (*11*). Not only their spectral proximity but also their similar optical densities at high spectral resolution assure very similar light-path lengths whose errors can be assumed to be below 0.5% (*11*). Due to the relatively coarse spatial resolution (60*30 km), we often encounter partially clouded pixels that might have the strongest influence on the light-path distribution. However, due to the spectral proximity of both retrieval windows, the cloud and surface albedo can be assumed to be the same resulting in equal light-paths even in the presence of partial cloud cover. Due to uncertainties in the instrumental slit function, the accuracy is currently estimated to be 10% but will improve in the future. We hitherto scaled our retrieved CH_4 VMR by 0.93 to adjust the measurements to column VMRs from the model that, in turn, is in

close agreement with ground-based measurements of surface VMRs from the NOAA/CMDL network (*S7,S8*). The systematic bias in the satellite observations is most probably related to uncertainties in the width of the instrumental slit function. Nevertheless, the bias does not affect the spatial variations shown in this paper.

Usually, measurements of oxygen (O_2 or O_4) (*S6,S9*) are used for the determination of column averaged mixing ratios (*S10*) since the O_2 VMR is known exactly. However, the spectral retrieval window for suitable O_2 detection (about 765 nm) is not near those of CO_2 or CH_4, creating larger uncertainties due to differences in the respective photon paths, especially in the presence of partial cloud cover or large aerosol loading in the field of view.

For the determination of the threshold line in Fig. 1a, we used a CO_2 VCD that corresponds to an effective cloud top height of approx. 1 km. This theoretical value was computed using a scale height of 8.5 km, which results in a maximum reduction of the expected CO_2 column (also computed with a scale height of 8.5 km) of 11%. This ensures that we probe the largest part of the atmospheric column (89%) and still use a reasonable fraction of available measurements (in our case approx. 20%).

The global chemistry-transport model TM3 (*15*) is used in this study at a spatial resolution of 2.5º x 2.5º with 31 vertical layers up to the 10-hPa pressure level. Six-hourly meteorological fields from the European Centre for Medium Range Weather Forecast (ECMWF) operational data are employed. These fields include global distributions for horizontal wind, surface pressure, temperature, humidity, liquid and ice water content, cloud cover and precipitation. Key processes included are mass-conserved tracer advection, convective tracer transport, boundary-layer diffusion, photolysis, dry and wet deposition as well as tropospheric chemistry including non-methane hydrocarbons to account for chemical loss by reaction with OH (*S11*). Methane emissions closely follow (15) (see also Figures S1, Table S1). Other emission distributions are based on the inventories from EDGAR (Emission Database

for Global Atmospheric Research) (*17*). CH_4 concentrations at the highest model level are nudged to the monthly-mean zonal HALOE/CLAES climatology from UARS (*S12*).

Supporting text

To examine the discrepancy between model and measurements over the tropical rainforest, we analyzed several possible influencing factors. The first possibility, a systematic error in the measured ratios, can be excluded. No correlation of the retrieval with albedo was found. Further, a possible retrieval bias dependent on solar zenith angle would lead to a strictly latitudinal dependence, whereas Fig. 3b shows considerable longitudinal variability in the tropics. Strong aerosol loading have also proven not to influence the ratio: Even in the presence of dust storms over the Sahara with very coarse aerosols that alter the light path also in the near infrared substantially, we found exactly the same light-path change (indicated by a change in the retrieved column) for both retrievals. This is mainly because the phase function and the optical density of the aerosols do not differ much between the two retrieval windows. Furthermore, both CH_4 and CO_2 exhibit similar optical densities, causing similar path-lengths even if aerosol scattering leads to a light-path distribution that depends on the optical density itself.

The second possibility, a systematic error in the model, can also be excluded. An underestimation of stratospheric methane concentrations would also result in a bias that mainly varies with latitude. Although most of the destruction of methane by OH radicals takes place in the tropical troposphere, a bias in the OH field (*S13*), possibly caused by strong emissions of non-methane hydrocarbons from the tropical rainforest in the dry season (*S14*), cannot explain the discrepancy either: A model simulation in which all OH over the tropical rainforest was removed caused an increase in methane concentrations of 0.7% at most, showing that an error in OH could explain only a very small fraction of the discrepancy.

Supporting Figures

Fig. S1:

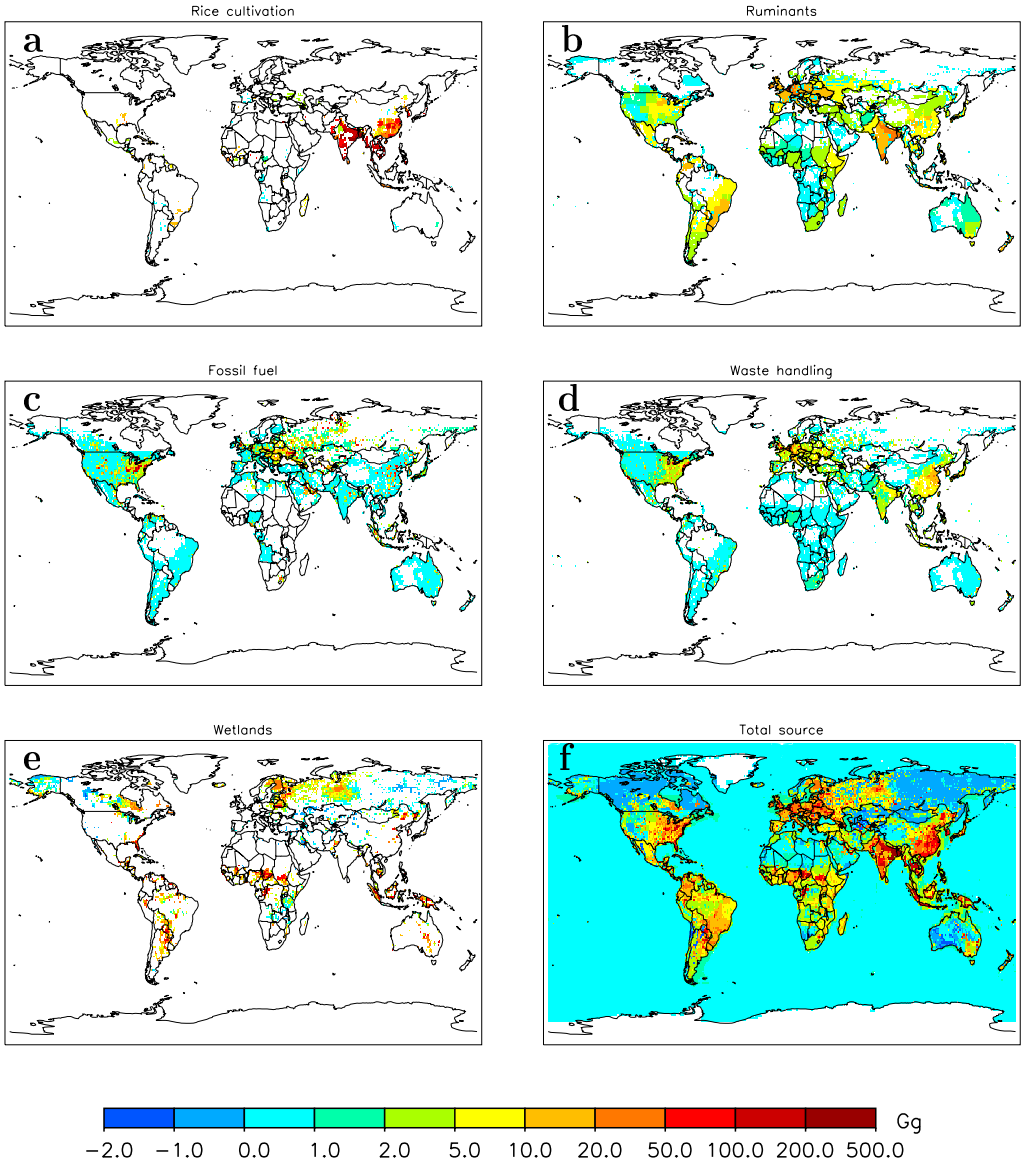

Fig. S1: Spatial distributions of the main methane sources as used in the TM3 model run (brackets contain the total strengths - in Tg CH_4 - from August through November, and over the whole year, respectively): (a) rice cultivation (42, 80), (b) ruminants (31, 93), (c) fossil-fuel production and transmission (30, 89), (d) waste handling (22, 65), (e) wetlands (48, 145), and (f) total source (192, 540). The emissions have been summed over the period August through November, and are shown on a 1°x1°- grid in units of Gg CH_4 per grid cell.

Fig. S2:

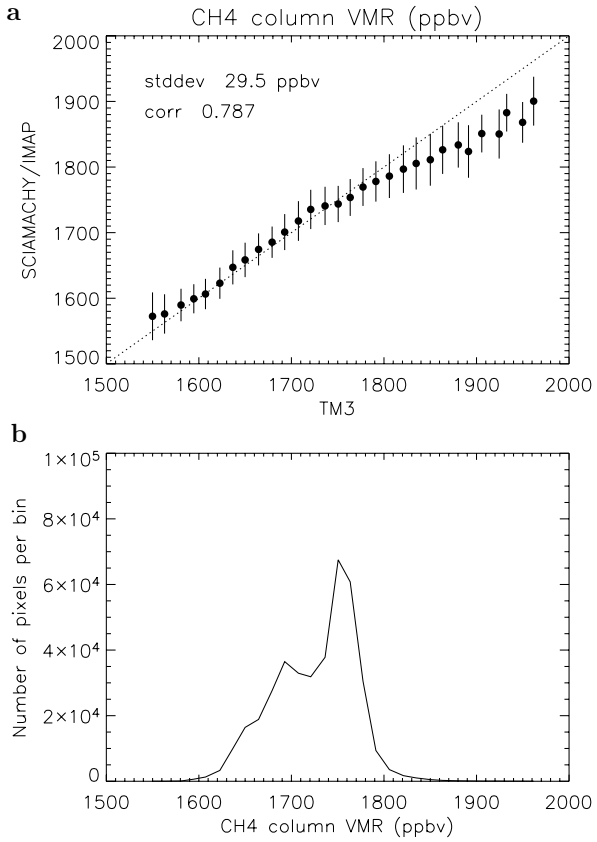

Fig. S2: Panel (a): Comparison of measured and modelled column-averaged VMR. The TM3 data have been averaged over bins of 15 ppbv. Corresponding SCIAMACHY averages over these bins are shown together with the ±1-sigma spread within each bin. The dotted line corresponds to the unit gradient line. Values of the standard deviation of the measurement-model difference, and of the linear (Pearson) correlation coefficient are given in the plot. The agreement between measurement and model is generally very good. In particular, the spread of measured concentrations relative to modelled ones is small (below 2%). Note that the relatively large mismatch at the highest concentrations represents only a small number of pixels (10-1000 for the highest 10 bins). However, there appear to be two clear explanations for this

discrepancy. First, the extreme model values are all sampled in South-East Asia, where the model presumably has a high bias due to an overestimation of the rice emissions. Second, the satellite pixel can contain some clouds, so that a fraction of the methane in the boundary layer may be shielded. This effect is largest when there is a lot of boundary-layer methane, i.e. in regions with large sources. Panel (b): Number of pixels per VMR-bin.

Fig. S3:

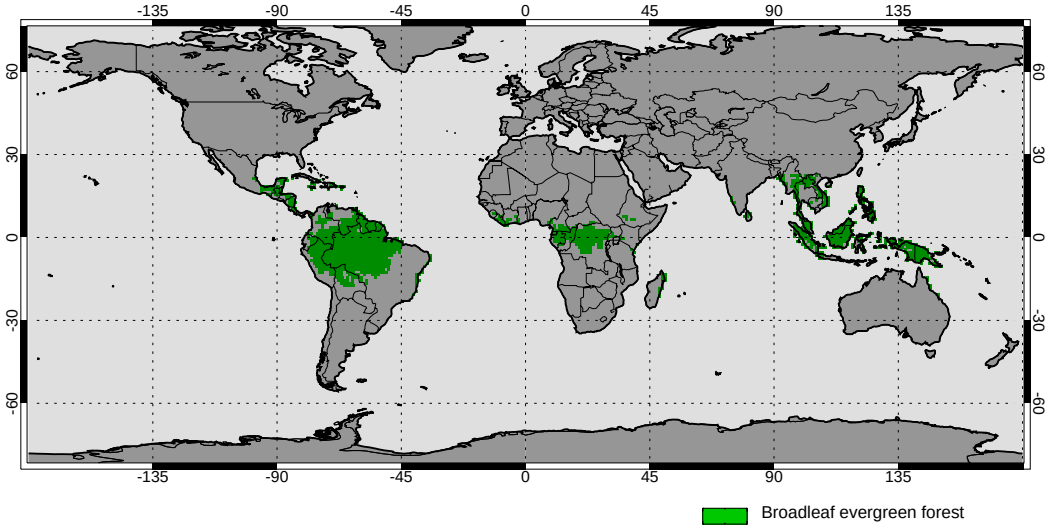

Fig. S3: Broadleaf evergreen forest is indicated in green (22)

Fig. S4:

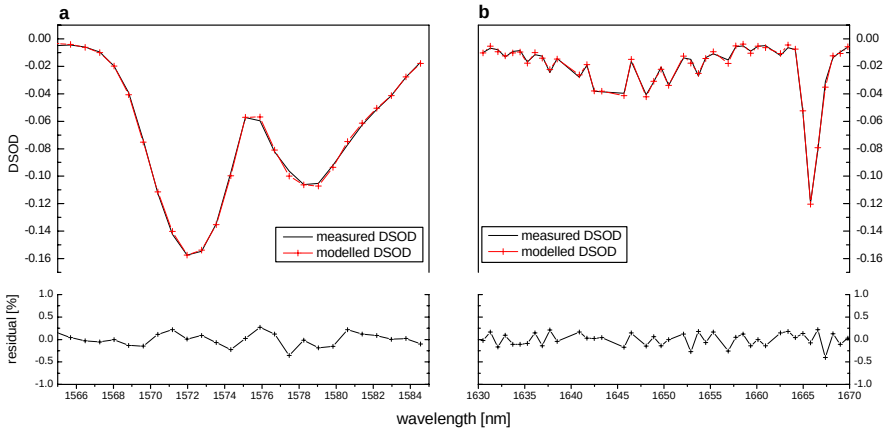

Fig. S4: Typical modelled and measured differential slant optical densities (DSOD) in the CO_2 (a) and CH_4 (b) fit windows are shown here. In panel (a), CO_2 contributes most to the depicted total DSOD, while there are also faint absorptions by water vapour. In panel (b), absorptions by CO_2 and H_2O marginally add to the strong CH_4 signal. In both panels, all species are fitted simultaneously and make up the total DSOD using a gaussian slit function with 1.35 nm full width at half maximum.

Supporting tables

Table S1: Methane emissions (Tg CH_4) per source category as used in the TM3 model for the period August through November 2003 and for the whole year (between brackets). The sources are given for six different regions: the whole globe, the tropics ($15^oS – 15^oN$), tropical Africa (30^oW-65^oE), tropical Indonesia (90^oE-180^oE), tropical South-America (180^oW-30^oW), and the Amazon basin (here taken as the area 15^oS-4^oN and 76^oW-50^oW).

Category	Globe	Tropics	Trop. Africa	Trop. Indon.	Trop. S-Amer.	Amazon
Fossil fuel production	29.8 (89.3)	1.3 (3.8)	0.2 (0.6)	0.7 (2.1)	0.4 (1.1)	0.0 (0.0)
Ruminants	31.1 (93.0)	5.2 (15.5)	2.2 (6.5)	0.6 (1.7)	2.0 (5.9)	0.3 (1.0)
Rice cultivation	41.5 (80.0)	5.9 (15.8)	0.7 (1.8)	3.7 (11.0)	0.3 (0.8)	0.0 (0.1)
Waste handling	21.7 (64.9)	1.6 (4.7)	0.5 (1.4)	0.5 (1.4)	0.5 (1.4)	0.0 (0.1)
Biomass burning	8.4 (29.0)	5.3 (16.7)	1.7 (7.9)	0.9 (2.2)	2.7 (6.5)	1.9 (3.6)
Biofuel burning	6.7 (20.0)	2.2 (6.6)	1.0 (3.1)	0.7 (2.1)	0.2 (0.7)	0.0 (0.1)
Other anthropogenic	1.7 (5.2)	0.0 (0.1)	0.0 (0.0)	0.0 (0.0)	0.0 (0.1)	0.0 (0.0)
Wetlands	47.7 (145.1)	23.5 (68.5)	12.0 (28.7)	7.1 (25.1)	4.3 (14.6)	1.9 (7.7)
Termites	6.7 (20.0)	4.2 (12.5)	2.1 (6.4)	0.5 (1.4)	1.5 (4.6)	0.9 (2.8)
Other natural	7.9 (23.5)	2.3 (6.8)	0.4 (1.2)	1.1 (3.2)	0.7 (2.2)	0.1 (0.3)
Soil sink	-11.0 (-30.0)	-3.5 (-10.1)	-1.9 (-5.5)	-0.4 (-1.3)	-1.2 (-3.2)	-0.6 (-1.5)
Total	192.2 (540.0)	47.8 (140.9)	18.9 (52.2)	15.3 (48.9)	11.5 (34.6)	4.6 (14.2)

Supplementary References

1. C. Rodgers, *Rev. Geophys. Space Phys.* **14**, 609 (1976).
2. C.D. Rodgers, *Inverse Methods for Atmospheric Sounding* (World Scientific, London, 2000).
3. L. Rothman *et al,. J. Quant. Spectrosc. Radiat. Transfer* **82**, 5 (2003).
4. R. Washenfelder, P. Wennberg, G. Toon, *Geophys. Res. Lett.* **30**, 2226 (2003).
5. P.J. Rayner, D.M. O'Brien, *J. Geophys. Res.* **107**, 4354 (2002).
6. K. Pfeilsticker, F. Erle, O. Funk, H. Veitel, U. Platt, J. Geophys. Res. 103, 11483 (1998).
7. E.J. Dlugokencky et al., Geophys. Res. Lett. 30 (19), 10.1029/2003GL018126 (2003).
8. E.J. Dlugokencky, K.A. Masarie, P.M. Lang, P.P. Tans, *Nature 393*, 447 (1998).
9. T. Wagner, J. Heland, M. Zöger, U. Platt, Atmos. Chem. Phys. 3, 651, 2003.
10. M. Buchwitz et al., Atmos. Chem. Phys. Discuss. accepted (2004).
11. S. Houweling, F.J. Dentener, J. Lelieveld, *J. Geophys. Res.* **103**, 10673 (1998).
12. UARS (Upper Atmosphere Research Satellite) CH_4 climatology: http://haloedata.larc.nasa.gov
13. M.G. Lawrence, P.Jöckel, R. von Kuhlmann, Atmos. Chem. Phys. 1, 37 (2001).
14. J. Kesselmeier *et al., J. Geophys. Res.* **107**, 8053 (2002).